

Original Article

Compensating Local Magnifications in Atom Probe Tomography for Accurate Analysis of Nano-Sized Precipitates

Robert Lawitzki* , Patrick Stender and Guido Schmitz

Institute of Materials Science, Department of Materials Physics, Universität Stuttgart, Heisenbergstraße 3, D-70569 Stuttgart, Germany

Abstract

Local magnification artifacts in atom probe tomography (APT) caused by multiphase materials with heterogeneous evaporation behavior are a well-known problem. In particular, the analysis of the exact size, shape, and composition of small precipitates is, therefore, not trivial. We performed numerical simulations of APT measurements to predict the reconstructed morphology of precipitates with contrasting evaporation thresholds. Based on a statistical approach that avoids coarse graining, the simulated data are evaluated to develop a model for the calculation of the original size of the precipitates. The model is tested on experimental APT data of precipitates with a higher and lower evaporation field in a ferritic alloy. Accurate sizes, proven by a complementary investigation by transmission electron microscopy, are obtained. We show further, how the size information can be used to obtain compositional information of the smallest precipitates and present a new methodology to determine a correct in-depth scaling of the APT reconstruction in case no complementary geometric information about the specimen exists or if no lattice planes are visible in the reconstruction.

Key words: atom probe tomography, cluster search, iron alloys, local magnification artifacts, simulation

(Received 4 January 2021; revised 9 February 2021; accepted 19 February 2021)

Introduction

Atom probe tomography (APT) is an analytical microscopy technique with up to single atom sensitivity in all three dimensions. A needle-shaped specimen with an apex radius of ~50–150 nm is subjected to a high DC voltage. By controlled voltage or laser pulsing, individual atoms are field desorbed from the surface and accelerated toward a position-sensitive detector, where the time of flight and the impact position are recorded (Cerezo et al., 1988; Blavette et al., 1993). After the measurement, the evaporated volume of the tip is reconstructed from the detected events to reveal the structural arrangement of the atoms inside the material. Since the exact ion trajectories are not known from the experiment, this reconstruction of the emitter is only possible by assumptions of the emitter's surface during field evaporation.

In most experimental works, the reconstruction follows a simple point projection model assuming a hemispherical apex (Bas et al., 1995). However, in the case of multiphase materials with varying evaporation threshold, the real tip shape changes during the measurement and the projection on a spherical emitter leads to significant distortions in the reconstruction known as local magnification artifacts (Miller & Hetherington, 1991; Miller et al., 1996). Though the composition of features in the APT reconstruction may not be severely affected by local

magnifications, the size of embedded nano-precipitates can deviate significantly (Vurpillot et al., 2000), which also explains why APT is often not applied to obtain size information. There have been several attempts in improving the reconstruction protocol pertaining to a hemispherical emitter (Gault et al., 2011b, 2011c; Suram & Rajan, 2013), but concepts with nonspherical symmetry that are capable to correct for local magnification artifacts during the measurement are rare. De Geuser et al. (2007) proposed an iterative reconstruction procedure that accounts for the difference in evaporation behavior of different phases, after the phases have been identified, and thereby homogenizes the volume laterally. Also, a reconstruction approach based on an analytical description of the emitter curvature for axial symmetric cases of bilayers (Rolland et al., 2015a) and multilayers (Rolland et al., 2015b) has been proposed. Another promising reconstruction approach by Fletcher et al. (2020) utilizes a 3D continuum model-driven reconstruction algorithm. Most recently, Beinke & Schmitz (2019) and Beinke et al. (2020) demonstrated a concept to extract the real shape of the emitter directly from the event density on the detector that is applicable to sample surfaces of almost arbitrary shape.

As an alternative to improving the reconstruction, one may use simulations of the evaporation process to predict the emitter shape, to correlate the simulated results with the experimental data, and to identify the required correction. Inspired by the work of Vurpillot et al. (1999), several groups developed simulation models and sequentially calculated ion trajectories of desorbing atoms determined by the highest field or polarization force until each atom has been removed from the model emitter

*Author for correspondence: Robert Lawitzki, E-mail: robert.lawitzki@mp.imw.uni-stuttgart.de

Cite this article: Lawitzki R, Stender P, Schmitz G (2021) Compensating Local Magnifications in Atom Probe Tomography for Accurate Analysis of Nano-Sized Precipitates. *Microsc Microanal* 27, 499–510. doi:10.1017/S1431927621000180

© The Author(s), 2021. Published by Cambridge University Press on behalf of the Microscopy Society of America. This is an Open Access article, distributed under the terms of the Creative Commons Attribution licence (<http://creativecommons.org/licenses/by/4.0/>), which permits unrestricted re-use, distribution, and reproduction in any medium, provided the original work is properly cited.

(Geiser et al., 2009; Larson et al., 2011; Marquis et al., 2011; Oberdorfer et al., 2013). Applications of these simulation approaches (e.g., Vurpillot et al., 2000; Oberdorfer et al., 2015) have improved the understanding of artifacts caused by local magnification and trajectory overlaps in atom probe measurements.

The necessary computation time to simulate a respective emitter and to derive the necessary parameters for the correction of the local magnification effects is extensive, whereas the conventional reconstruction approach is very fast, in comparison. Therefore, it would be still beneficial to use the point projection protocol applying generally valid quantitative corrections to the size and composition values of precipitates that were determined from the erroneous reconstruction. Such a correction becomes especially important when the size of the precipitates scales down to less than 5 nm. A first approach that utilizes an analytical model with parameters derived from ion-trajectory simulations and which accounts for spatial overlaps near-phase interfaces due to local magnification effects was proposed by Blavette et al. (2001) and enabled to correct the apparent composition of spherical precipitates with a lower evaporation field.

Utilizing this idea, we simulated the field evaporation of emitters with embedded spherical precipitates with the versatile simulation package *TAPSim* (Oberdorfer et al., 2013) and analyzed the size, shape, and atomic density of the reconstructed precipitates by a statistical approach. Based on these numerical data, we developed a model to calculate the correct size of precipitates that appeared locally magnified or compressed in the APT reconstruction. The applicability of the concept is demonstrated on APT measurements of a ferritic alloy containing NiAl-type precipitates. It is further shown that the concept can be extended to also determine the composition of the precipitates avoiding the use of composition profiles or proxigrams (Hellman et al., 2000) and even to optimize the in-depth scaling of the APT reconstruction.

Experimental

The ferritic alloy FBB-8 designed by Teng et al. (2010) which is strengthened by ordered NiAl-type precipitates was chosen to demonstrate the effect of local magnifications on the reconstruction of small precipitates. Two differently heat-treated alloys were analyzed complementarily by transmission electron microscopy (TEM) and APT. Additionally, a series of APT simulations were set up to study the influence of the evaporation behavior of spherical precipitates embedded in a matrix on the reconstruction after field evaporation. Finally, a statistical approach is presented to analyze the size and shape of reconstructed precipitates in simulated and experimental APT datasets.

Alloy Details

An ingot of the ferritic alloy FBB-8 with a nominal composition of Fe-12.7Al-9Ni-10.2Cr-1.9Mo-0.14Zr (in atomic percentage) was prepared using raw materials of at least 99.99% purity in an arc melting furnace and subsequently solution treated for 30 min at 1,200°C sealed in quartz tubes under an argon atmosphere. After solution treatment, the ingot was quenched in water and cut into 2-mm-thick slices for isothermal heat treatments at 700 and 800°C in pre-heated tube furnaces (in air atmosphere). After 50 h, the samples were removed from the furnace. During the subsequent cooling in air to room temperature, nano-sized NiAl-type (cooling) precipitates formed, which have shown in a previous study (Lawitzki et al., 2021), to precipitate in B2

structure when cooling from 800°C but in a metastable (Pnma) structure when cooling from 700°C.

Experimental Details

Samples for the investigation by TEM and APT were prepared by FIB lift-out with a dual-beam FEI SCIOS FIB-SEM and fixed for TEM to a copper grid provided by PELCO® and for APT by fixation of a blank to a tungsten post and subsequent annular milling (Giannuzzi & Stevie, 1999; Miller & Russell, 2007). The TEM specimens were investigated with a Philips CM-200 FEG TEM operated at 200 kV in a dark-field (DF) mode. In order to obtain the best contrast between the NiAl-type ordered precipitates and the matrix, the specimens were aligned in a two-beam condition close to a low indexed zone axis and tilted to intensify a specific superlattice reflection (e.g., [001]-zone axis with {010}-reflection intensified).

The APT analysis of the samples heat treated at 800°C were performed in a noncommercial femtosecond laser-assisted local electrode tomographic atom probe (TAP; Schlesiger et al., 2010). The TAP was operated with a pulse frequency of 200 kHz using a laser power of 33 mW (with a spot size of ~60 µm giving a pulse energy of 150 nJ) while cooling the specimen to 50 K.

The samples heat treated at 700°C were analyzed in a noncommercial wide-angle tomographic atom probe (WATAP; Stender et al., 2007) by applying voltage pulses with a repetition rate of 75 kHz, a pulse fraction of 20% (a pulse width of 5 ns), and a 120 mm delay line detector. In order to obtain a higher throughput of long measurements, the specimen temperature was increased to 80 K.

The APT reconstruction was performed with the software *Scito* (Balla & Stender, 2019) according to the protocol by Bas et al. (1995) which requires the detection efficiency (here 50%), the average evaporation field and the field compression factor as input parameters.

For the laser-pulsed measurement, the evaporation field was determined by first measuring the number of 1+ and 2+ ions for specific elements, calculating their ratio and referencing the post-ionization theory by Haydock & Kingham (1980) and Kingham (1982) and the ionization energies given in Tsong's review (Tsong, 1978). The field was determined to be an average of 22 V/nm for the Cr, Fe, and Ni ions. In the case of the voltage pulsed measurement, the evaporation field of pure iron of 33 V/nm was used (Gault et al., 2012); the lack of 1+ charged ions in the mass spectrum clearly indicated a higher evaporation field of atoms in the voltage pulsed measurement. The choice of the field compression factor influences the scaling of the *z* (in-depth) dimension of the reconstruction and is usually adjusted by matching the distance of lattice planes in the reconstruction to those in the real material or by adjusting the reconstruction to the *a priori* known tip shape (or features in the tip) investigated by complementary electron microscopy. In the discussion part, a new method for the choice of the field compression factor is presented.

Precipitates were searched with the *maximum separation algorithm* (Heinrich et al., 2003; Vaumousse et al., 2003) with Ni as the marker species. The critical distance d_{\max} was derived from the tenth nearest neighbor distance distribution and set to the first maximum of the double-peaked distribution, which stems from distances within the precipitates (Lawitzki et al., 2021). The surfaces of the identified clusters were Delaunay triangulated, allowing the calculation of proxigrams of the elemental

distribution and atomic density in shells of constant thickness around the convex hull, even in the case of nonspherical shape.

Atom Probe Simulations

Full-scale simulations of APT measurements were performed with the simulation package TAPSim (Oberdorfer et al., 2013, 2015), which is, in comparison with other approaches, not restricted to regular meshes. Needle-shaped tips with a radius of 9 nm, a length of 35 nm, and a shaft angle of 5° with a bcc mesh (lattice parameter of 0.2886 nm) containing about 0.8 million grid points (~1.5 million grid points when including additional support points) were constructed. The effect of a limited spatial resolution of APT was modeled by randomly shifting atoms laterally by ± 0.2 nm and in-depth by ± 0.05 nm in half width, which further avoids complications by crystalline faceting. The microstructure of the field emitters was set up to match the particular experimental situation in the ferritic alloy: Six tips containing a matrix of 5.8 at.% solute atoms and one centralized spherical precipitate of different radii (1.2, 1.7, 2.2, 2.7, 3.2, and 4.1) nm containing 44.0 at.% solute atoms. The emitters were then field evaporated by the calculation of the desorption probabilities from the polarization forces. The field evaporations of each of these model emitters were simulated seven times with varying contrast in the evaporation thresholds between matrix atoms ($E_\alpha = 20.0$ V/nm) and precipitate atoms ($E_\beta = 16.0, 17.2, 20.0, 22.8, 24.0, 25.2$, or 27.3 V/nm) yielding in total 42 simulations. The simulated 2D detector data were reconstructed with a reconstruction protocol that fixes the initial radius and shaft angle of the emitter (Jeske & Schmitz, 2001).

Methods

A Statistical Approach for the Size Analysis

Since extracting the size and shape of nano-precipitates directly from an APT reconstruction (e.g., by evaluation of the volume within an isosurface) depends strongly on the coarse-graining process and the user-defined interface between the precipitate and the matrix (Barton et al., 2019), the size of precipitates is easily over- or underestimated if too many or too few atoms are considered as belonging to the precipitate. An alternative method is to calculate the radius of gyration r_g from the coordinates of the constituent atoms i by

$$r_g = \sqrt{\frac{\sum_{i \in N} r_i^2}{N}}, \quad (1)$$

where N is the number of atoms in the precipitate and $r_i = \bar{x}_i - \bar{x}_S$ is the distance of an individual atom \bar{x}_i from the center of mass \bar{x}_S (Miller, 2000; Miller & Kenik, 2004). However, for a precipitate embedded in a matrix that consists of the same atomic species only with a different composition, the number of atoms in the precipitate N is unknown and cannot be extracted directly from the APT data without defining the precipitate interface. A quantity that could be accessed instead is the number of excess atoms Γ . Consider a larger volume consisting of A and B atoms surrounding a single precipitate. The B atoms may represent the decomposing solute atoms. They may have a matrix concentration $c_{0,B}$. Then, the number of excess atoms Γ_B due to the embedded

precipitate is calculated by

$$\Gamma_B = \sum_{j \in B} (1 - c_{0,B}) - \sum_{i \in A} (c_{0,B}) = N_B(1 - c_{0,B}) - N_A c_{0,B}, \quad (2)$$

where N_A and N_B are the total number of A and B atoms, respectively, in the volume. Similarly, equation (1) can be generalized to determine the radius of gyration r_g without identifying the atoms of the precipitate by

$$r_g = \sqrt{\frac{\sum_{j \in B} (1 - c_{0,B})(\bar{x}_j - \bar{x}_S)^2 - \sum_{i \in A} (c_{0,B})(\bar{x}_i - \bar{x}_S)^2}{\Gamma_B}}, \quad (3)$$

where the center of mass \bar{x}_S is given by

$$\bar{x}_S = \frac{\sum_{j \in B} (1 - c_{0,B})\bar{x}_j - \sum_{i \in A} (c_{0,B})\bar{x}_i}{\Gamma_B}. \quad (4)$$

For homogeneous spherical precipitates, the radius of gyration r_g is related to the more intuitively interpreted sphere radius R (Guinier, 1963) by

$$R = \sqrt{\frac{5}{3}} r_g. \quad (5)$$

In order to solve equations (2)–(5), the concentration $c_{0,B}$ of solute atoms B in the bulk phase has to be known. A possibility to determine this concentration $c_{0,B}$ from atoms in vicinity of the precipitate is, to express equation (2) as a function of an offset $\Delta c_{0,B}$

$$\Gamma_B^{\text{calc}} = N_B(1 - c_{0,B} - \Delta c_{0,B}) - N_A(c_{0,B} + \Delta c_{0,B}), \quad (6)$$

$$\Leftrightarrow_{(2)} \Gamma_B^{\text{calc}} = \Gamma_B - (N_B + N_A)\Delta c_{0,B} = \Gamma_B - N_{\text{tot}}\Delta c_{0,B}, \quad (7)$$

where N_{tot} is the total number of atoms in any analysis volume that includes the precipitate completely. As the excess must be independent of the chosen volume, the linear relation on $\Delta c_{0,B}$ expressed in equation (7) may be evaluated for volumes of different size (see Fig. 1a), and thus different N_{tot} . The correct bulk concentration and excess are found as the crossing of the linear graphs produced of differently sized volumes. This is demonstrated in Figure 1b, where the bulk concentration $c_{0,B}$ and the excess Γ_B are directly obtained from the intersection. It should be mentioned that in real APT measurements, the calculated excess by equation (7) is reduced by the detection efficiency. As a caveat, it has to be further mentioned here that, while increasing the volume, one has to carefully avoid including parts of another particle.

Analysis of Aspect Ratios and Relative Density Ratios

Precipitates with a different evaporation field with respect to the surrounding bulk appear typically compressed or expanded laterally in the APT reconstruction due to local magnification artifacts. The change in morphology of the reconstructed precipitates is, in the following, described in terms of their aspect ratio and the ratio

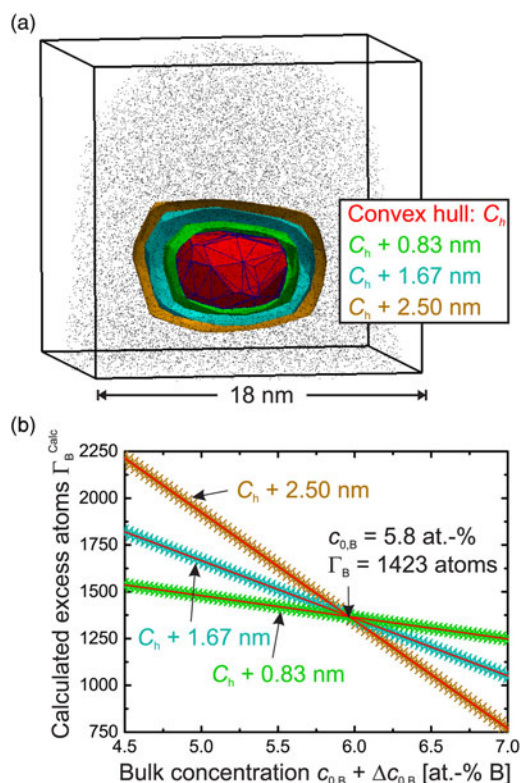


Fig. 1. A method to determine the number of excess atoms B belonging to a precipitate in an atom probe dataset: (a) atom probe reconstruction of the model tip showing only B atoms containing a precipitate with an original radius of 2.2 nm. For illustration, precipitate atoms were identified by cluster search and triangulated to present their convex hull (red). Volumes of three arbitrary shells around the precipitate ($C_h + x$) were cropped and used for generating the diagram in (b): calculated excess atoms Γ_B^{calc} as a function of the bulk concentration ($c_{0,B} + \Delta c_{0,B}$) for three differently sized shells (red solid lines) merge in one point that represents the correct choice.

of the atomic densities inside and outside the precipitate. The aspect ratio Φ_{AR} of the reconstructed precipitates is obtained by equation (3), when the radius of gyration is evaluated in the x -, y -, and z -directions separately which allows to define

$$\Phi_{AR} := \frac{1/2(r_g(x) + r_g(y))}{r_g(z)}. \quad (8)$$

To calculate the density ratios Φ_{DR} between reconstructed precipitates (β') and the surrounding α matrix

$$\Phi_{DR} := \rho_{\alpha}/\rho_{\beta'}, \quad (9)$$

concentric spherical shells are positioned around the center of mass of a precipitate (equation (4)) and their atomic densities are determined. Plotting these densities versus the shell radius and extrapolating to the center ($R \rightarrow 0$) and far off the precipitate $R \rightarrow \infty$ the densities inside the precipitates $\rho_{\beta'}$ and inside the matrix in vicinity of the precipitates ρ_{α} are evaluated. In this work, we isolated the precipitates by cluster search with the maximum separation method.

Results

The Model to Correct Size and Shape of Precipitates in APT Volume Reconstructions

Numerical simulations of APT measurements of emitters containing a spherical precipitate were performed to study the artifacts in the morphology of the precipitate. For transparency, only the results of the emitters containing the precipitate with an initial radius of 2.2 nm are demonstrated in Figure 2, a comparison of the results of all 42 simulations is given in the Supplementary material. In Figure 2 (and in Supplementary Figs. S1–S3), phase and density maps of the simulated field

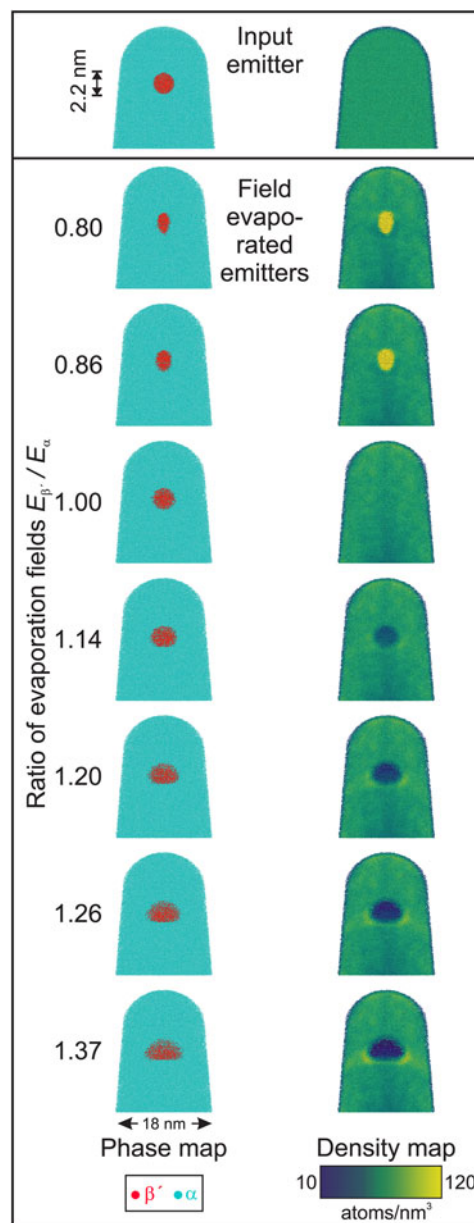


Fig. 2. Comparison of phase maps (left) and atomic density distribution maps (right) of APT reconstructions from datasets obtained by simulated field evaporation. The simulations were performed with different ratios between the evaporation thresholds of the matrix and the precipitate as stated at the left. The model emitter contained a precipitate sized 2.2 nm in radius. In the top row, the original input structure of the simulation is shown.

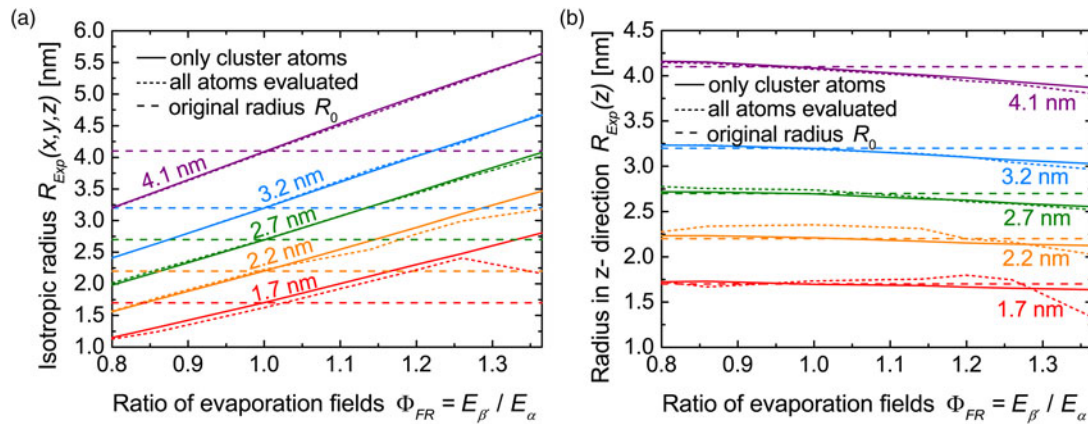


Fig. 3. Comparison of the isotropic radii $R_{Exp}(x, y, z)$ (a) and the radii in the z-direction $R_{Exp}(z)$ (b) of the precipitates in dependence of the ratio of evaporation fields Φ_{FR} . The solid lines are the radii obtained when considering only the precipitate atoms for the evaluation (only possible for simulated emitters, in which the origin of all atoms can be identified) and dotted lines, when matrix atoms are considered as well in the evaluation. Dashed lines indicate the original precipitate radii R_0 .

emitters are presented in dependence on the ratio between the evaporation thresholds

$$\Phi_{FR} = E_{\beta} / E_{\alpha}, \quad (10)$$

between precipitate (pure β) and matrix phase (pure α). As already shown by other authors (Vurpillot et al., 2000, 2004; Oberdorfer et al., 2015; Hatzoglou et al., 2017; Beinke & Schmitz, 2019), field evaporated precipitates with $\Phi_{FR} > 1$ show an expansion and those with $\Phi_{FR} < 1$ a compression in their size, mainly in the lateral direction. Furthermore, it is shown that the density distribution around the precipitate is not homogeneous and the geometry of the reconstructed precipitate is rather complex and not simply ellipsoidal.

In Figure 3, the evaluated radii R_{Exp} of the reconstructed precipitates are compared in the dependence of the ratio of evaporation fields. The radii obtained by considering cluster atoms only (solid lines), calculated by equations (1) and (5) are compared with the radii evaluated, considering both matrix and precipitate atoms in a larger volume, calculated by equations (3) and (5) (dotted lines). Both methods deliver almost identical results (solid and dotted lines). Only for clusters with radii of less than 2.7 nm and with very large ratios Φ_{FR} , do deviations become noticeable, which are caused by statistical fluctuations.

Since the precipitates are not spherical after field evaporation (cf. Fig. 2), the radii in the x- and y-directions differ from the radii in the z-direction. Therefore, the isotropic radii $R_{Exp}(x, y, z)$ (in Fig. 3a) are compared with those determined only in the z-direction $R_{Exp}(z)$ (Fig. 3b). The radius in the z-direction $R_{Exp}(z)$ delivers already rather good size estimates of the original precipitate radius R_0 (with a relative error of $\pm 3.0\%$ considering only cluster atoms and of $\pm 7.3\%$ considering all atoms). In contrast to this, $R_{Exp}(x, y, z)$ is not a suitable direct measure of the original precipitate size, since it strongly depends on the ratio between evaporation thresholds; only for $\Phi_{FR} = 1$, the isotropic radius $R_{Exp}(x, y, z)$ equals the original radius and confirms the validity of equation (5). Since the in-depth scaling of an APT reconstruction, and therefore the z-dimension of the precipitates, depends strongly on the reconstruction parameters (e.g., like the field compression factor or the detector efficiency), a conclusion from $R_{Exp}(z)$ to R_0 is nevertheless doubtful if the in-depth scaling cannot be proven by an independent method. For this reason, we

develop here a model to calculate the original cluster radii R_0 from the isotropic radii $R_{Exp}(x, y, z)$ that allows an accurate size estimate even if the in-depth scaling is not correct (which will be shown in the discussion part below).

In Figure 3a, the isotropic radii $R_{Exp}(x, y, z)$ show linear dependences, with slope m_1 , on the ratio of evaporation fields Φ_{FR} and no deviation to the original radii R_0 for $\Phi_{FR} = 1$. This suggests a radius correction as

$$R_{Exp} = R_0 \cdot f(R_0, \Phi_{FR}) = R_0 [1 + m_1(R_0) \cdot (\Phi_{FR} - 1)]. \quad (11)$$

The size ratios of the isotropic and original radii $R_{Exp}(x, y, z) / R_0$, as shown in Figure 4, demonstrate that the slope $m_1(R_0)$ is a function of the original radius that converges to 1 for $R_0 \rightarrow \infty$. Indeed, the dependence of slope m_1 on the original radius R_0 can be approximated exponentially by

$$m_1(R_0) = 1 + a_1 \cdot \exp(-b_1 \cdot R_0), \quad (12)$$

where $a_1 = 2.78$ and $b_1 = 0.76$ (as shown in Supplementary Fig. S5a). Following equations (11) and (12), the original precipitate radii R_0 could be evaluated when the ratio of evaporation

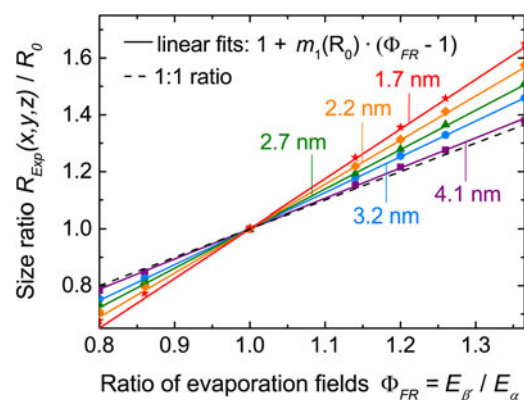


Fig. 4. Dependence of the size ratio between the isotropic radii $R_{Exp}(x, y, z)$ and the original radii R_0 versus the ratio in evaporation fields Φ_{FR} . The dashed line indicates a 1:1 correlation.

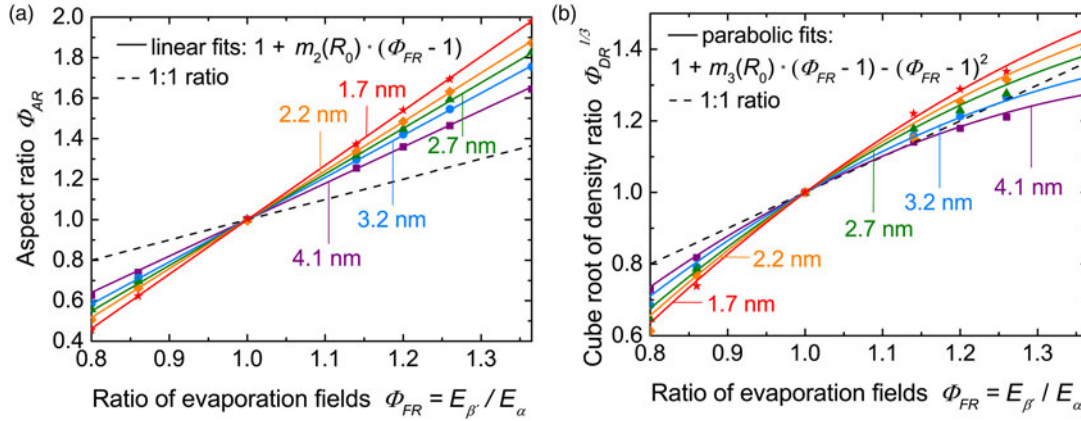


Fig. 5. Correlation between the aspect ratios Φ_{AR} (a) and the cubic root of the density ratios (b) of the reconstructed precipitates and the ratio in evaporation fields Φ_{FR} . The dashed lines indicate a 1:1 correlation.

fields Φ_{FR} is known (cf. the three-dimensional graph in Supplementary Fig. S4).

To determine Φ_{FR} , a second quantity describing the cluster morphology that depends on the original size and the ratio of evaporation fields is necessary. Both, the aspect ratios Φ_{AR} (equation (8)) and the density ratios Φ_{DR} (equation (9)) are suitable candidates for this.

As presented in Figure 5a, the aspect ratios Φ_{AR} also follow a linear dependence on the ratio of evaporation fields (analogously to the size ratios) and can, therefore, be described by

$$\Phi_{AR} = 1 + m_2(R_0) \cdot (\Phi_{FR} - 1) \Leftrightarrow \Phi_{FR} - 1 = \frac{\Phi_{AR} - 1}{m_2(R_0)}, \quad (13)$$

where $m_2(R_0)$ is again approximated exponentially as in equation (12) with $a_2 = 2.82$ and $b_2 = 0.30$ (as shown in Supplementary Fig. S5b). Considering equations (11) and (13), now the isotropic radius R_{Exp} can be described by

$$R_{Exp} = R_0 \cdot f(R_0, \Phi_{AR}) = R_0 \cdot \left[1 + \frac{(1 + a_1 \cdot \exp(-b_1 \cdot R_0))}{(1 + a_2 \cdot \exp(-b_2 \cdot R_0))} \cdot (\Phi_{AR} - 1) \right], \quad (14)$$

which can be solved numerically for the original radii R_0 after measurement of the isotropic radii R_{Exp} and the aspect ratios Φ_{AR} .

In Figure 6b, the dependence of the cubic root of the density ratios Φ_{DR} on Φ_{FR} is presented. Under the assumptions that precipitates β' and matrix phase α have the same initial density ($\rho_\alpha = \rho_{\beta'_0}$) and that the density of the matrix ρ_α is properly reproduced in the reconstruction, the density ratios Φ_{DR} , as defined by equation (9), can be rewritten as

$$\Phi_{DR} = \frac{\rho_{\beta'_0}}{\rho_{\beta'_{Exp}}} = \frac{V_{Exp}}{V_0} \approx \frac{R_{Exp}^3}{R_0^3} \Leftrightarrow \sqrt[3]{\Phi_{DR}} \approx \frac{R_{Exp}}{R_0}, \quad (15)$$

where V_0 and V_{Exp} are the volumes of the precipitates before field evaporation and in the reconstruction. Equation (15) indicates that the cubic root of the density ratios should show the same behavior as the size ratios between the isotropic and original radii $R_{Exp}(x, y, z)/R_0$ as presented in Figure 4. However, from Figure 5b, it is obvious that $\Phi_{DR}^{1/3}$ cannot be described solely by

a linear function (e.g., by an analog to equation (13)) but when additionally subtracting a quadratic dependence on the ratios of evaporation fields Φ_{FR}

$$\sqrt[3]{\Phi_{DR}} = 1 + m_3(R_0) \cdot (\Phi_{FR} - 1) - (\Phi_{FR} - 1)^2, \quad (16)$$

a well matching description is achieved, where $m_3(R_0)$ is again approximated exponentially as in equation (12) with $a_3 = 2.15$ and $b_3 = 0.16$ (as shown in Supplementary Fig. S5c). A possible explanation for the quadratic term in equation (16) is seen in the change of the morphology of the clusters. Since the clusters are not spherical, and not even ellipsoidal, in the reconstruction, the approximation of $V \propto R_{Exp}^3$ is not accurate anymore. This is demonstrated in Supplementary Figure S6 where the isotropic radius $R_{Exp}(x, y, z)$ is compared with the equivalent radius R_{Ellips}

$$R_{Ellips} = \sqrt[3]{R_{Exp}(x) \cdot R_{Exp}(y) \cdot R_{Exp}(z)}, \quad (17)$$

when assuming an ellipsoidal cluster shape. Equation (16) can be rewritten as

$$\Phi_{FR} - 1 = \frac{1}{2} \left(m_3(R_0) \pm \sqrt{4 + m_3(R_0)^2 - 4 \cdot \sqrt[3]{\Phi_{DR}}} \right), \quad (18)$$

and by considering equations (11) and (18), now the isotropic radius R_{Exp} can be described by

$$R_{Exp} = R_0 \cdot f(R_0, \Phi_{DR}) = R_0 \cdot \left[1 + m_1(R_0) + \frac{1}{2} \left(m_3(R_0) - \sqrt{4 + m_3(R_0)^2 - 4 \cdot \sqrt[3]{\Phi_{DR}}} \right) \right]. \quad (19)$$

Equation (19) allows calculating the original radii R_0 after measurement of the isotropic radii R_{Exp} and the density ratios Φ_{DR} .

In deriving the previous equations (14) and (19) that enable the calculation of the original precipitate radii R_0 , only the atoms indexed as a precipitate phase in the reconstructed emitters were considered to obtain a maximum in accuracy of the model. In Figure 6, corrected radii of the precipitates in the reconstructed

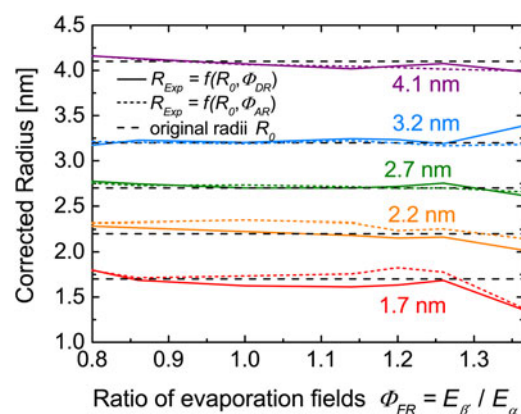


Fig. 6. Comparison of the radii of the reconstructed precipitates after correction using the measured isotropic radii R_{Exp} and the density ratios Φ_{DR} (solid lines) by equation (19), after correction using the measured isotropic radii R_{Exp} and the aspect ratios Φ_{AR} (dotted lines) by equation (14) to the original radii R_{Exp} in the dependence of the ratio in evaporation fields Φ_{FR} (dashed lines).

emitters have been calculated considering all atoms (situation in real experiments). Both approaches yield very good size estimates for precipitates ≥ 2.7 nm and with ratios in evaporation fields $\Phi_{FR} < 1.3$ (total deviation in size of less than 1.5%). Only for smaller precipitates and higher positive field ratios, statistical fluctuations may cause larger deviations to the original size ($\pm 3.6\%$ for 2.2-nm-sized clusters and $\pm 5.2\%$ deviation for 1.7-nm-sized clusters). The results of the smallest precipitates with a radius of 1.2 nm (containing only 266 excess atoms) are not shown in the diagrams since their size could not be evaluated to a precision better than $\pm 20\%$.

Tests with Experimental Data

The model for correction of precipitate sizes after local magnification or compression in APT reconstructions, as introduced in the previous section, is applied to APT measurements of a ferritic alloy containing nano-sized NiAl-type precipitates and compared with an evaluation by TEM in the following section.

Investigation by TEM

The existence of nano-sized ordered precipitates in both heat-treated samples of alloy FBB-8 was proven by TEM dark-field imaging (cf. Fig. 7). In the sample heat treated at 700°C (Fig. 7a), the precipitates are barely resolvable, in contrast, the situation after heat treatment at 800°C (Fig. 7b) shows that the spherical precipitates can be clearly identified. With the software *ImageJ* (Schneider et al., 2012), the bright areas of more than 100 precipitates in each state were manually overlaid by circles enabling the estimation of mean radii. After heat treatment at 700°C, a mean radius of (1.7 ± 0.3) nm, and after heat treatment at 800°C, a mean radius of (6.2 ± 1.2) nm for the ordered precipitates were obtained. Since the contrast of small precipitates is not homogeneously bright, but rather fades out at the edges, the radii evaluated by TEM DF imaging strongly depend on how the surface of a precipitate is defined, indicating further that conventional TEM cannot give a more precise answer here. Additionally, no clear information on the composition by energy dispersive X-ray (EDX) spectroscopy or by electron energy loss spectroscopy (EELS) can be obtained, because the signal of

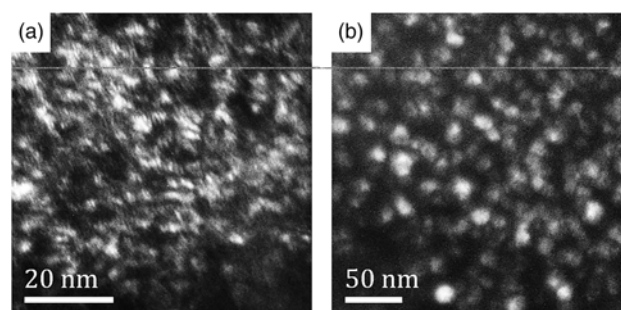


Fig. 7. Dark-field TEM images of ordered NiAl type precipitates (white contrast) in the alloy FBB-8 after heat treatment at 700°C (a) and 800°C (b).

small precipitates cannot be deconvoluted from the surrounding matrix.

In Figure 8, the reconstructions of two APT tips after heat treatment at 800°C (Fig. 8a) and 700°C (Fig. 8b) are compared. The precipitates are visualized by isosurfaces (25 at.% Ni). Consistent with the results evaluated by TEM (see Fig. 7), the cooling precipitates are larger after heat treatment at 800°C. (The large precipitate also seen in Fig. 8b is part of a primary precipitate that exhibits a precipitate free zone around it.) In the reconstruction, the cooling precipitates have a lower atomic density than the matrix and appear compressed in the measurement direction when the specimen was cooled from 800°C (Fig. 8a). Surprisingly, after heat treatment at 700°C, they show the opposite behavior appearing more stretched in the measurement direction and have a higher atomic density (Fig. 8b and later Fig. 10). Since these precipitates naturally exhibit a spherical shape (cf. TEM images in Fig. 7) and are coherent to the matrix (with the same density), it is obvious that their APT reconstructions must have been influenced by local magnification artifacts, or possibly by a general erroneous scaling of the reconstruction, and therefore serve as an ideal example to test the presented model to evaluate the precipitates' original sizes. Following the conclusions from the performed APT simulations, the precipitates reconstructed with a lower density after heat treatment at 800°C have a higher evaporation threshold than the matrix atoms ($\Phi_{FR} > 1$) and vice versa, after heat treatment at 700°C, precipitates are expected to have a lower evaporation threshold ($\Phi_{FR} < 1$).

Precipitates with a Higher Evaporation Threshold than the Bulk

For the measurement represented in Figure 8a, five analysis boxes containing one precipitate each were cropped and further analyzed. First, the maximum separation method for cluster detection was applied for Ni atoms, allowing representation of the precipitate by a convex hull and calculation of the composition and density in the vicinity of the triangulated surface. As shown by the proxigram in Figure 8a, in this case of still rather large precipitates, a quantification of the fraction of Ni in the core of the precipitate (44 at.%) is best obtained by the fit with an error function (see also Table 1). On the contrary, the fraction of Ni would be underestimated, when calculating the Ni fraction from all atoms within the convex hull (33.5 at.%) because of a contribution of matrix atoms in the interface region.

The isotropic radius $R_{Exp}(x, y, z)$ of each precipitate was then analyzed by the presented statistical approach (equation (5)) and applied to calculate the original radius R_0 by considering the density ratios Φ_{DR} (equation (19)). From the number of excess atoms Γ_B , the density $\rho_{\beta'}$, and the radius $R_{\beta'}$ of the precipitate, the

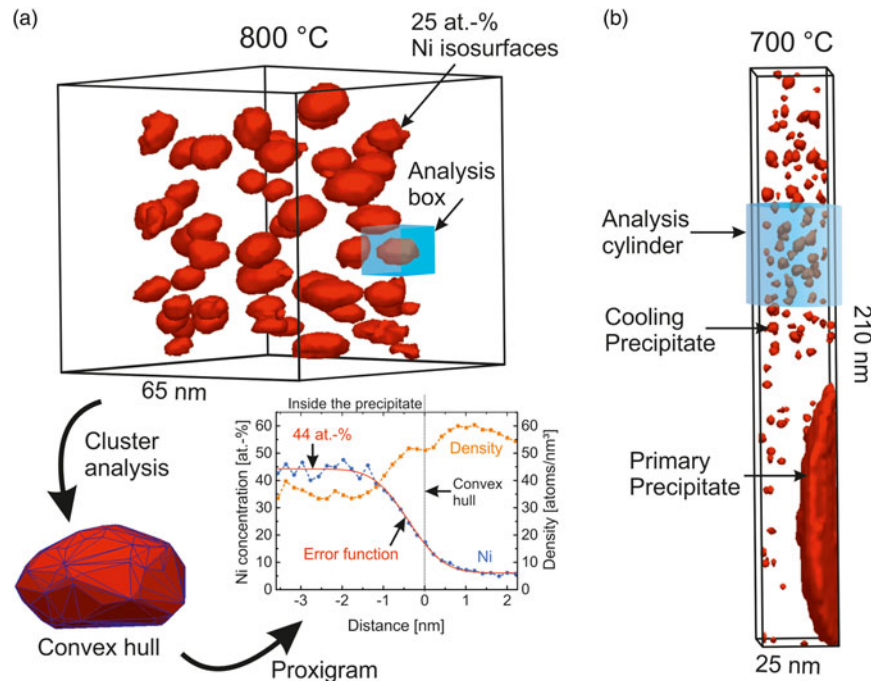


Fig. 8. Reconstruction of two atom probe tips visualized by 25 at.-% Ni isosurfaces after heat treatment of the alloy FBB-8 at 800 °C **(a)** and 700 °C **(b)**; regions containing NiAl-type cooling precipitates (analyses boxes) were cropped to further study the cooling precipitates by cluster analysis and calculating proxigrams as shown in **(a)**.

concentration of B atoms in the precipitate $c_{\beta'}$ can be calculated by

$$c_{\beta'} = \frac{\Gamma_B}{\rho_{\beta'} \cdot (4/3)\pi R_{\beta'}^3} + c_{0,B}, \quad (20)$$

where $c_{0,B}$ is the concentration of solute atoms B in the matrix. Since the precipitates and matrix have the same density in the alloy FBB-8, the matrix density ρ_{α} has to equal the density of the precipitates $\rho_{\beta'}$ in the alloy. The obtained concentration $c_{\beta'}$ is not reduced by the limited detection efficiency, since both the

number of excess atoms Γ_B and the measured density ρ_{α} are reduced by the detection efficiency. On the other hand, the limited detection efficiency reduces the accuracy of the analysis, especially for small precipitates. Equation (20) can be applied to all elements which are enriched (show a positive excess) within the precipitate.

The concentration $c_{\beta'}$ can now be compared with the concentrations obtained from the proxigram and allows to cross-check, whether the size estimation was reasonable (cf. Table 1). In view of the data in the table, it becomes clear that both the size directly obtained from the convex hulls R_{CH} , as well as the isotropic radius R_{Exp} overestimate the real size of the precipitate.

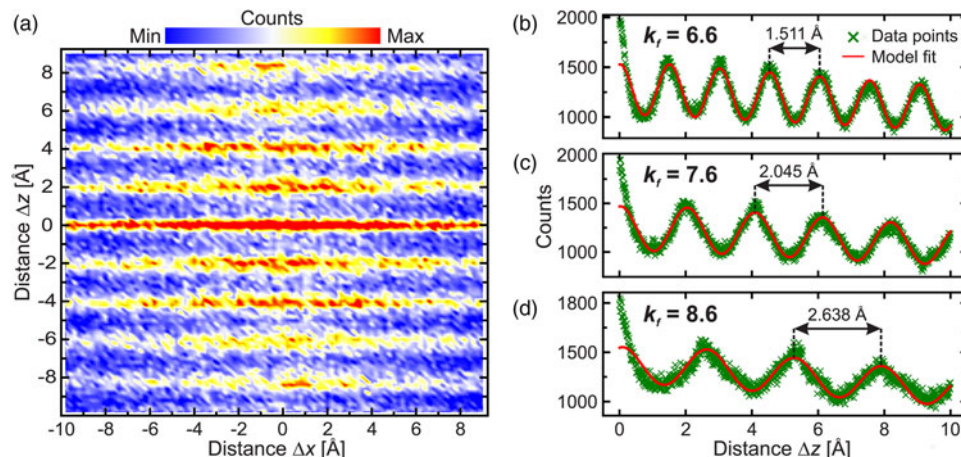


Fig. 9. **(a)** Spatial distribution map (SMD) in the x - and z -direction of atoms close to a zone axis in the sample heat treated at 700 °C; **(b–d)** radial distribution maps obtained by averaging the SDM in the z -direction and applying different field compression factors k_r of 6.6 **(b)**, 7.6 **(c)**, 8.6 **(d)** in the APT reconstruction. The data points were fitted by a sum of Gaussian functions.

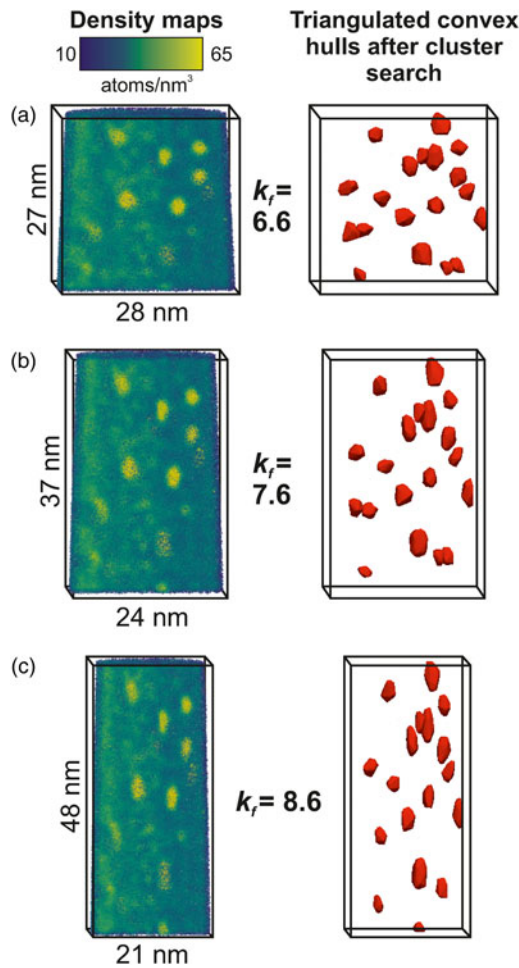


Fig. 10. Density maps (left) and detected precipitates after use of the maximum separation algorithm and visualized by their triangulated convex hulls (right) of one APT dataset reconstructed by applying three different field compression factors k_f of 6.6 (a), 7.6 (b), and 8.7 (c).

However, when using the observed density ratio for the calculation of the ratio in evaporation thresholds Φ_{FR} by equation (18) ($\Phi_{DR} = 1.14 \pm 0.05$) and applying this to calculate the original radii R_0 equation (19), the evaluated composition differs in average by only ± 2.6 at.% Ni compared with the composition obtained from the proxigram. Consequently, the corrected size is convincingly close to the real size of the precipitate.

Precipitates with a Lower Evaporation Threshold than the Bulk
The second example (Fig. 8b) shows precipitates with a lower evaporation threshold that leads to a higher reconstructed density (see also Fig. 10). One cylinder over the complete width of the tip and with 37 nm in length containing 19 precipitates was cropped and further analyzed. After precipitate localization by cluster search and statistical size analysis of each individual cluster, the averaged isotropic mean radius R_{Exp} of (1.45 ± 0.23) nm was determined. Applying equation (19), an original mean radius R_0 of (1.80 ± 0.31) nm with an average ratio in evaporation thresholds Φ_{FR} of (0.83 ± 0.03) was calculated by considering the measured density ratios, which is very close to the radius evaluated by TEM, (1.7 ± 0.3) nm. Applying equation (20) to calculate the fraction of Ni in the precipitate yields a concentration of (73 ± 16) at.% Ni using the isotropic radius R_{Exp} but (43.7 ± 7.0) at.% Ni when using the correctly calculated original radius R_0 . The comparison of these concentrations to the average of (40.2 ± 2.1) at.% Ni obtained by evaluating all 19 proxigrams demonstrates the quality of the size corrected radius which only allows a realistic determination of the composition. Furthermore, this is a very clear example to demonstrate the impact of a small evaporation threshold on the volume of the reconstructed precipitate which is only half of the real volume of the precipitate.

Discussion

The presented examples have demonstrated that the original size of locally magnified or compressed precipitates in APT reconstructions can be correctly derived by considering the isotropic radii and the density ratios by equation (19). For the simulated tips in the section “Analysis of aspect ratios and relative density ratios”, it was shown that instead of the density ratios, also the aspect ratios equation (14) can be used for the calculation of the original precipitate radii. In this work, both methods to determine the original size of the precipitates have been tested with the result that the calculations using the density ratios performed better; especially for the large clusters presented in Figure 8a. The main reason for this is that the aspect ratio of the reconstructed precipitates depends very strongly on the quality of the APT reconstruction. A derivation of the assumed hemispherical tip shape, for example, due to crystallographic effects during reconstruction (Nakamura & Kuroda, 1969; Waugh et al., 1975; Oberdorfer & Schmitz, 2011), modifies the reconstructed shape of the precipitates relative to the direction of a zone axis. Furthermore, the scaling of the z-dimension (measurement direction) of the APT tip depends on the field compression factor k_f .

Table 1. Comparison of the Evaluated Radii and Atomic Fractions of Ni Atoms of Five Different Precipitates after Heat Treatment at 800°C Obtained by Different Analysis Methods.

Precipitate	Radius (nm)			Atomic Fraction of Ni Atoms (at.%)			
	From Convex Hull R_{CH}	Isotropic Radius R_{Exp}	Calc. Original Radius R_0	From Convex Hull	Calc. from R_{Exp}	Calc. from R_0	From Proxigram
1	5.23	5.36	4.42	33.2	27.6	44.3	43.2
2	5.25	5.53	4.85	38.9	32.4	45.3	47.7
3	4.77	4.93	4.15	33.5	26.6	40.0	44.0
4	3.55	3.73	3.38	36.1	33.5	43.3	48.2
5	4.70	4.83	4.05	34.1	26.5	40.2	42.9

Table 2. Analysis of the APT Measurement of the Sample Heat Treated at 700°C Reconstructed by Applying Three Different Field Compression Factors k_f . Compared are the lattice plane distances evaluated by spatial distribution maps (SDM) and the closest theoretical lattice plane distance of the bcc Fe-alloy, the field ratios Φ_{FR} derived by the aspect ratios Φ_{AR} (equation (13)) and the density ratios Φ_{DR} (equation (18)), the isotropic radius $R_{Exp}(x, y, z)$ and the calculated original radii $R_0(\Phi_{AR})$ (equation (14)) and $R_0(\Phi_{DR})$ (equation (19)) and the elemental concentration of Ni derived from the proxigrams and calculated with equation (20) applying the corrected radii estimates of the precipitates.

Field Compression Factor k_f		6.6	7.6	8.6
Lattice plane distance d_{hkl} (nm)	Measured by SDM	0.1511	0.2045	0.2638
	Nearby d_{hkl} in Fe-alloy	$d_{111}:0.1666, d_{200}:0.1443$	$d_{110}:0.2041$	$d_{110}:0.2041$
Field ratio Φ_{FR}	Using Φ_{AR}	0.93 ± 0.10	0.83 ± 0.06	0.74 ± 0.13
	Using Φ_{DR}	0.830 ± 0.028	0.835 ± 0.029	0.828 ± 0.032
Radius (nm)	$R_{Exp}(x, y, z)$	1.40 ± 0.04	1.45 ± 0.06	1.62 ± 0.05
	$R_0(\Phi_{AR})$	1.36 ± 0.06	1.79 ± 0.11	2.32 ± 0.12
	$R_0(\Phi_{DR})$	1.75 ± 0.05	1.83 ± 0.08	2.02 ± 0.08
Ni concentration (at.%)	Proxigram		40.2 ± 2.1	
	Corrected by Φ_{AR}	84.6 ± 2.4	43.7 ± 2.9	26.6 ± 1.9
	Corrected by Φ_{DR}	43.3 ± 2.1	43.4 ± 1.7	32.5 ± 1.6

which is a user-defined parameter in the APT reconstruction protocol (Bas et al., 1995). A common practice to derive this parameter is by tuning k_f until either the geometry of (or the arrangement of features in) the APT reconstruction matches to the *a priori* known shape determined by correlative electron microscopy (Larson et al., 1999; Arslan et al., 2008; De Geuser et al., 2008; Gault et al., 2011a), or if visible, by matching the distance of reconstructed lattice planes with those in the real material (Gault et al., 2012). If none of these methods can be applied, which was the case for the example shown in Figure 8a, a reconstruction with a correct in-depth scaling is so far not possible. Nonetheless, the size estimation of precipitates derived from the density ratios has shown to be a reliable measure of the evaporation thresholds of different species yielding accurate compositions, even if the in-depth scaling might not have been absolutely correct. A generalization of this approach to originally ellipsoidal (or other convex) shaped precipitates appears possible but still is to be tested in future studies.

In the APT reconstruction of the measurement performed with the voltage-pulsed atom probe (WATAP) (Fig. 8b), a better in-depth resolution was obtained and lattice planes became visible which are identified by the spatial distribution map (SDM) technique (Moody et al., 2009) in Figure 9a. Since 2D desorption maps have not revealed any clear zone axis or zone lines, an easy identification of the zone axis is not possible. Therefore, we performed several reconstructions with a variation in the field compression factor k_f as presented in Figures 9b–9d and Figure 10, where k_f was varied from 6.6 (a), to 7.6 (b), to 8.6 (c). In Figure 10, the atomic density of the reconstructed tips (left) and the triangulated convex hulls of precipitates after cluster search by the maximum separation method (right) are compared. The lattice plane distance can be extracted from small regions ($4 \times 4 \times 6 \text{ nm}^3$) around the zone axis by averaging the SDMs in the z -direction, as presented in Figures 9b–9d, and increases from 0.151 nm (b), to 0.205 nm (c), to 0.264 nm (d).

Based on the shown experimental data, there is seemingly no method to decide, which of the three APT reconstructions is best. Naively, one could choose the field compression factor k_f (according to Fig. 10a), so that precipitates become spherical in the reconstruction and thereby ignoring local magnification

effects. However, the more realistic solution can be found, when comparing the field ratio Φ_{FR} obtained from the aspect ratios Φ_{AR} (equation (13)) to the field ratio determined from the density ratios Φ_{DR} (equation (18)), as shown in Table 2. Whereas Φ_{AR} is strongly influenced by a variation in the field compression factor, Φ_{DR} is constant for all three reconstructions and, therefore, is an independent measure of the field ratio Φ_{FR} of ~ 0.83 . Only for $k_f = 7.6$, the field ratios obtained from Φ_{AR} or Φ_{DR} are equal, indicating that this field compression factor is the most realistic one. When comparing the evaluated lattice plane distances (see Figs. 9b–9d) to the theoretical distances in the bcc lattice of alloy FBB-8 (cf. Table 2), a distance of 0.2638 nm for $k_f = 8.6$ is far off from any theoretical distance ($d_{110} = 0.2041$ nm is the closest one) and also a distance of 0.1511 nm for $k_f = 6.6$, does not clearly represent a specific lattice plane family in the ferritic alloy ($d_{111} = 0.1666$ nm and $d_{200} = 0.1443$ nm are closest). But for $k_f = 7.6$, the measured lattice plane distance of 0.2045 nm agrees well with the distance of (110) planes ($d_{110} = 0.2041$ nm). Furthermore, this field compression factor of 7.6 is confirmed when comparing the Ni concentration evaluated by equation (20) from the calculated radii of the precipitates (43.7 at.% by Φ_{AR} and 43.4 at.% by Φ_{DR}) to the concentration that is obtained by averaging all individual proxigrams (40.2 at.%). For $k_f = 6.6$ and 8.6, the erroneously evaluated radius by the aspect ratios (1.75 or 2.02 nm, respectively) results in a strongly overestimated (84.6 at.% for $k_f = 6.6$) or underestimated (26.6 at.% for $k_f = 8.6$) amount in Ni. This example shows that the presented model for size evaluation of precipitates in APT datasets can be even applied to tune the field compression factor and, therefore, offers a new possibility to find the optimum in-depth scaling of APT measurements without prior knowledge of the APT tips shape and the visibility of lattice planes in the APT reconstruction.

Conclusions

Numerical simulations were performed to study the influence of the field evaporation behavior of spherical nano-sized precipitates embedded in a matrix in APT measurements. A statistical analysis based on the evaluation of excess atoms of the precipitates

revealed the following relations to the ratio in evaporation thresholds between the matrix and precipitate atoms:

- a linear relation with the isotropic radius derived from the gyration radius of the precipitates;
- a linear relation to the aspect ratio of the precipitates; and
- a quadratic relation to the cubic root of the density ratio of the precipitate and matrix densities.

With the observed relations, a model was developed to evaluate the original size of locally magnified or compressed precipitates. The model was tested on APT data of the ferritic alloy FBB-8 containing precipitates with either a higher (1.14 times) or lower (0.83 times) evaporation field compared with the surrounding bulk depending on the heat treatment. Complementary measurements by TEM and additional tests have shown that the size information after size correction with the proposed model are reliable.

Furthermore, it was shown that the proposed model can be used to tune the APT reconstruction parameters to find a correct in-depth scaling for cases where no lattice planes are visible in the APT reconstruction and no complementary information on the APT tip (shape) exists. It is also recommended as an independent method to evaluate the difference in evaporation thresholds of matrix and precipitates.

Supplementary material. To view supplementary material for this article, please visit <https://doi.org/10.1017/S1431927621000180>.

Acknowledgments. This work was supported by the German Research Foundation (grant numbers: SCHM 1182/19-2, HO 3322/3-1, WA 3818/1-1, and KR 3687/3-1). We thank Thomas Meisner and Arnold Weible for their assistance in the alloy fabrication, Daniel Beinke for the assistance in developing model datasets, and Sebastian Eich for the help on the spatial distribution mapping analysis.

References

- Arslan I, Marquis EA, Homer M, Hekmaty MA & Bartelt NC (2008). Towards better 3D reconstructions by combining electron tomography and atom-probe tomography. *Ultramicroscopy* **108**, 1579–1585.
- Balla I & Stender P (2019). Scito. Available at <http://inspico.de/Software/Reconstruction-Scito/> (retrieved October 8, 2020).
- Barton DJ, Hornbuckle BC, Darling KA & Thompson GB (2019). The influence of isoconcentration surface selection in quantitative outputs from proximity histograms. *Microsc Microanal* **25**, 401–409.
- Bas P, Bostel A, Deconihout B & Blavette D (1995). A general protocol for the reconstruction of 3D atom probe data. *Appl Surf Sci* **87–88**, 298–304.
- Beinke D, Bürger F, Solodenko H, Acharya R, Klauk H & Schmitz G (2020). Extracting the shape of nanometric field emitters. *Nanoscale* **12**, 2820–2832.
- Beinke D & Schmitz G (2019). Atom probe reconstruction with a locally varying emitter shape. *Microsc Microanal* **25**, 280–287.
- Blavette D, Bostel A, Sarrau JM, Deconihout B & Menand A (1993). An atom probe for three-dimensional tomography. *Nature* **363**, 432–435.
- Blavette D, Vurpillot F, Pareige P & Menand A (2001). A model accounting for spatial overlaps in 3D atom-probe microscopy. *Ultramicroscopy* **89**, 145–153.
- Cerezo A, Godfrey TJ & Smith GDW (1988). Application of a position-sensitive detector to atom probe microanalysis. *Rev Sci Instrum* **59**, 862–866.
- De Geuser F, Gault B, Stephenson LT, Moody MP & Muddle BC (2008). Atom probe tomography calibration through post-analysis considerations. In *51st International Field Emission Symposium (IFES)*, Rouen, France. Available at <https://hal.archives-ouvertes.fr/hal-01838927>.
- De Geuser F, Lefebvre W, Danoix F, Vurpillot F, Forbord B & Blavette D (2007). An improved reconstruction procedure for the correction of local magnification effects in three-dimensional atom-probe. *Surf Interface Anal* **39**, 268–272.
- Fletcher C, Moody MP & Haley D (2020). Towards model-driven reconstruction in atom probe tomography. *J Phys D: Appl Phys* **53**, 475303.
- Gault B, de Geuser F, Bourgeois L, Gabbie BM, Ringer SP & Muddle BC (2011a). Atom probe tomography and transmission electron microscopy characterisation of precipitation in an Al–Cu–Li–Mg–Ag alloy. *Ultramicroscopy* **111**, 683–689.
- Gault B, Haley D, de Geuser F, Moody MP, Marquis EA, Larson DJ & Geiser BP (2011b). Advances in the reconstruction of atom probe tomography data. *Ultramicroscopy* **111**, 448–457.
- Gault B, Loi ST, Araullo-Peters VJ, Stephenson LT, Moody MP, Shrestha SL, Marceau RKW, Yao L, Cairney JM & Ringer SP (2011c). Dynamic reconstruction for atom probe tomography. *Ultramicroscopy* **111**, 1619–1624.
- Gault B, Moody MP, Cairney JM & Ringer SP (2012). *Atom Probe Microscopy*. New York, NY: Springer New York. Available at <http://link.springer.com/10.1007/978-1-4614-3436-8>.
- Geiser B, Larson D, Gerstl S, Reinhard D, Kelly T, Prosa T & Olson D (2009). A system for simulation of tip evolution under field evaporation. *Microsc Microanal* **15**, 302–303.
- Giannuzzi LA & Stevie FA (1999). A review of focused ion beam milling techniques for TEM specimen preparation. *Micron* **30**, 197–204.
- Guinier A (1963). *X-Ray Diffraction in Crystals, Imperfect Crystals, and Amorphous Bodies*. San Francisco: W. H. Freeman and Company.
- Hatzoglou C, Radiguet B & Pareige P (2017). Experimental artefacts occurring during atom probe tomography analysis of oxide nanoparticles in metallic matrix: Quantification and correction. *J Nucl Mater* **492**, 279–291.
- Haydock R & Kingham DR (1980). Post-ionization of field-evaporated ions. *Phys Rev Lett* **44**, 1520–1523.
- Heinrich A, Al-Kassab T & Kirchheim R (2003). Investigation of the early stages of decomposition of Cu-0.7 at% Fe with the tomographic atom probe. *Mater Sci Eng A* **353**, 92–98.
- Hellman OC, Vandenbroucke JA, Rüsing J, Isheim D & Seidman DN (2000). Analysis of three-dimensional atom-probe data by the proximity histogram. *Microsc Microanal* **6**, 437–444.
- Jeske T & Schmitz G (2001). Nanoscale analysis of the early interreaction stages in Al/Ni. *Scr Mater* **45**, 555–560.
- Kingham DR (1982). The post-ionization of field evaporated ions: A theoretical explanation of multiple charge states. *Surf Sci* **116**, 273–301.
- Larson DJ, Geiser BP, Prosa TJ, Gerstl SSA, Reinhard DA & Kelly TF (2011). Improvements in planar feature reconstructions in atom probe tomography. *J Microsc* **243**, 15–30.
- Larson DJ, Russell KF & Miller MK (1999). Effect of specimen aspect ratio on the reconstruction of atom probe tomography data. *Microsc Microanal* **5**, 930–931.
- Lawitzki R, Beinke D, Wang D & Schmitz G (2021). On the formation of nano-sized precipitates during cooling of NiAl-strengthened ferritic alloys. *Mater Charact* **171**, 110722.
- Marquis EA, Geiser BP, Prosa TJ & Larson DJ (2011). Evolution of tip shape during field evaporation of complex multilayer structures. *J Microsc* **241**, 225–233.
- Miller MK (2000). *Atom Probe Tomography*. Boston, MA: Springer US. doi:10.1046/j.1365-2818.2001.00847.x
- Miller MK, Cerezo A, Hetherington MG & Smith GDW (1996). *Atom Probe Field Ion Microscopy*. Oxford: Oxford University Press.
- Miller MK & Hetherington MG (1991). Local magnification effects in the atom probe. *Surf Sci* **246**, 442–449.
- Miller MK & Kenik EA (2004). Atom probe tomography: A technique for nanoscale characterization. *Microsc Microanal* **10**, 336–341.
- Miller MK & Russell KF (2007). Atom probe specimen preparation with a dual beam SEM/FIB miller. *Ultramicroscopy* **107**, 761–766.
- Moody MP, Gault B, Stephenson LT, Haley D & Ringer SP (2009). Qualification of the tomographic reconstruction in atom probe by advanced spatial distribution map techniques. *Ultramicroscopy* **109**, 815–824.
- Nakamura S & Kuroda T (1969). On field-evaporation end forms of a bcc metal surface observed by a field ion microscope. *Surf Sci* **17**, 346–358.
- Oberdorfer C, Eich SM, Lüttemeyer M & Schmitz G (2015). Applications of a versatile modelling approach to 3D atom probe simulations. *Ultramicroscopy* **159**, 184–194.

- Oberdorfer C, Eich SM & Schmitz G** (2013). A full-scale simulation approach for atom probe tomography. *Ultramicroscopy* **128**, 55–67.
- Oberdorfer C & Schmitz G** (2011). On the field evaporation behavior of dielectric materials in three-dimensional atom probe: A numeric simulation. *Microsc Microanal* **17**, 15–25.
- Rolland N, Larson DJ, Geiser BP, Duguay S, Vurpillot F & Blavette D** (2015a). An analytical model accounting for tip shape evolution during atom probe analysis of heterogeneous materials. *Ultramicroscopy* **159**, 195–201.
- Rolland N, Vurpillot F, Duguay S & Blavette D** (2015b). Dynamic evolution and fracture of multilayer field emitters in atom probe tomography: A new interpretation. *Eur Phys J Appl Phys* **72**, 21001.
- Schlesiger R, Oberdorfer C, Würz R, Greiwe G, Stender P, Artmeier M, Pelka P, Spaleck F & Schmitz G** (2010). Design of a laser-assisted tomographic atom probe at Münster University. *Rev Sci Instrum* **81**, 043703.
- Schneider CA, Rasband WS & Eliceiri KW** (2012). NIH image to ImageJ: 25 years of image analysis. *Nat Methods* **9**, 671–675.
- Stender P, Oberdorfer C, Artmeier M, Pelka P, Spaleck F & Schmitz G** (2007). New tomographic atom probe at University of Muenster, Germany. *Ultramicroscopy* **107**, 726–733.
- Suram SK & Rajan K** (2013). Calibration of reconstruction parameters in atom probe tomography using a single crystallographic orientation. *Ultramicroscopy* **132**, 136–142.
- Teng ZK, Liu CT, Ghosh G, Liaw PK & Fine ME** (2010). Effects of Al on the microstructure and ductility of NiAl-strengthened ferritic steels at room temperature. *Intermetallics* **18**, 1437–1443.
- Tsong TT** (1978). Field ion image formation. *Surf Sci* **70**, 211–233.
- Vaumousse D, Cerezo A & Warren PJ** (2003). A procedure for quantification of precipitate microstructures from three-dimensional atom probe data. *Ultramicroscopy* **95**, 215–221.
- Vurpillot F, Bostel A & Blavette D** (2000). Trajectory overlaps and local magnification in three-dimensional atom probe. *Appl Phys Lett* **76**, 3127–3129.
- Vurpillot F, Bostel A, Menand A & Blavette D** (1999). Trajectories of field emitted ions in 3D atom-probe. *Eur Phys J Appl Phys* **6**, 217–221.
- Vurpillot F, Cerezo A, Blavette D & Larson DJ** (2004). Modeling image distortions in 3DAP. *Microsc Microanal* **10**, 384–390.
- Waugh AR, Boyes ED & Southon MJ** (1975). Field-desorption microscopy and the atom probe. *Nature* **253**, 342–343.